

## Apatite low-temperature chronometry and microstructures across a hydrothermally active fault zone

Alfons Berger<sup>a,\*</sup>, Daniel Egli<sup>a,b</sup>, Christoph Glotzbach<sup>c</sup>, Pierre G. Valla<sup>a,d</sup>, Thomas Pettke<sup>a</sup>, Marco Herwegh<sup>a</sup>

<sup>a</sup> Institute of Geological Sciences, University of Bern, Baltzerstrasse 1+3, CH-3012 Bern, Switzerland

<sup>b</sup> Kiefer and Studer AG, Burgstr. 12a, 4153, Reinach, Switzerland

<sup>c</sup> Department of Geosciences, University of Tuebingen, Schnarrenbergstr. 94-96, 72076 Tuebingen, Germany

<sup>d</sup> ISTerre, Univ. Grenoble Alpes, Univ. Savoie Mont Blanc, CNRS, IRD, IFRSTAR, 38000, Grenoble, France

### ARTICLE INFO

Editor: Balz Kamber

#### Keywords:

Apatite (U-Th)/He ages  
Hydrothermal systems  
Microstructures  
Trace element geochemistry  
Fault zones

### ABSTRACT

Low-temperature chronometers offer potential to gain insights into the temporal evolution of hydrothermal systems. The long-lived fault-bound Grimsel pass hydrothermal system (including a fossil and an active part) in the Central European Alps serves here as a key site to test such an application. Zircon and apatite grains were separated from samples collected along a fault transect. The resulting zircon (U-Th)/He ages are homogenous along the profile at 8–9 Ma and thus record the regional cooling evolution, remaining unaffected by the younger hydrothermal activity. In contrast, the apatite (U-Th)/He ages show three age groups: One Group (1) of ca. 5 Ma inside and outside the hydrothermal zone matches the low-temperature part of the regional cooling trend, while group (2) with ages as young as 1–2 Ma occurs in a central narrow zone associated with hydrothermal activity. One sample (group 3) displays older apparent ages compared to the regional cooling trend. Group (2) apatite samples reveal a different cathodoluminescence texture and trace-element chemistry, which we interpret together with the young age as apatite growth or re-crystallization within the hydrothermal system. Forward 1D modelling of He diffusion indicates that apatite (U-Th)/He ages should always be reset when exposed to hot thermal waters (up to ~140 °C) present over ka timescales or to intermediate temperature waters (~90 °C) over Ma timescales. Combining our measured apatite (U-Th)/He ages with forward modelling results highlight that, besides regional cooling trends, local heat anomalies within hydrothermal zones are very variable in space and time. Combined trace-element geochemistry and (U-Th)/He dating shows local occurrence of newly-formed apatites crystals, which are best described as geochronometers rather than thermochronometers. Such information is important to explore the longevity of hydrothermal systems and associated spatial distributions of heat anomalies.

### 1. Introduction

Rock cooling/exhumation signals can be well determined by low-temperature thermochronology methods such as the apatite and zircon fission-track (AFT and ZFT) or (U-Th)/He (AHe and ZHe) systems (Reiners and Brandon, 2006; Reiners et al., 2018, and references therein). More specifically low-temperature thermochronometry is a unique tool to estimate the timing for cooling below specific temperature ranges (e.g. ~60–90 °C for AHe; e.g., Shuster et al., 2006; Reiners et al., 2018). The thermal impact on fission-track annealing and helium diffusion in apatite has been studied in great detail and resulting

annealing and diffusion models can assist in deriving the cooling history of rocks (e.g., Flowers et al., 2009; Gautheron et al., 2009; Djimbi et al., 2015; Zeitler et al., 2017). Hydrothermal systems can modify the heat distribution in a rock mass and thereby disturb the above mentioned cooling/exhumation signal determined by low-temperature thermochronometers (Gorynski et al., 2014; Reiners et al., 2018, and references therein). Recent studies on hydrothermal systems associated with active tectonic faults have shown that AHe ages far away from faults record regional cooling, but closer to the fault, AHe ages may be perturbed (Whipp and Ehlers, 2007; Gorynski et al., 2014; Milesi et al., 2019, 2020). AHe ages may be (i) younger compared to the regional trend

\* Corresponding author.

E-mail address: [alfons.berger@geo.unibe.ch](mailto:alfons.berger@geo.unibe.ch) (A. Berger).

<https://doi.org/10.1016/j.chemgeo.2021.120633>

Received 6 May 2021; Received in revised form 7 November 2021; Accepted 11 November 2021

Available online 16 November 2021

0009-2541/© 2021 The Author(s). Published by Elsevier B.V. This is an open access article under the CC BY license (<http://creativecommons.org/licenses/by/4.0/>).

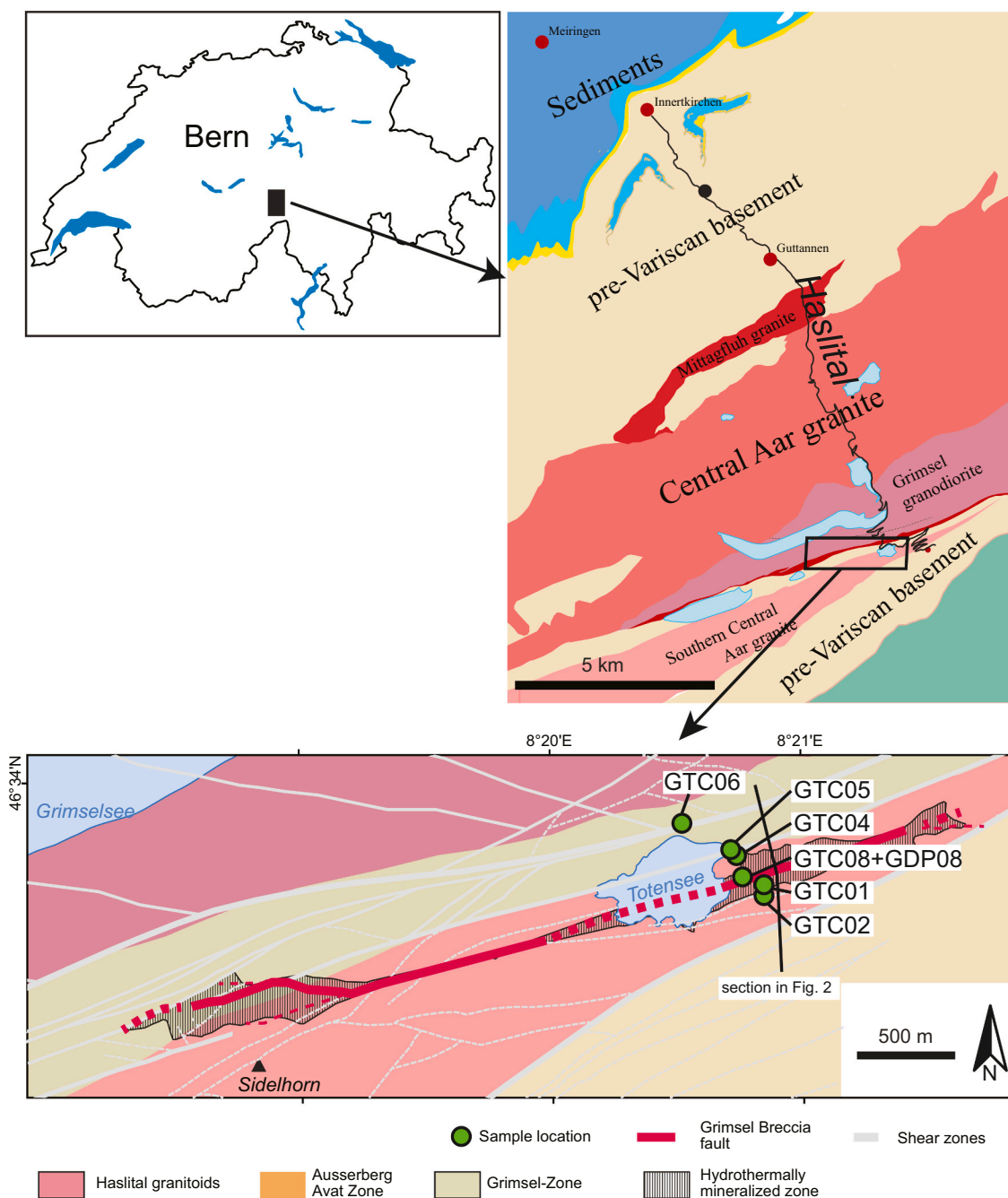


**Fig. 1.** Geological setting of the study area in the Swiss Alps indicating the major tectonic units and main tectonic lines, as well as the sample locations and the mapped extent of hydrothermal mineralization (after Belgrano et al., 2016 and Berger et al., 2017). Upper insets show location within Switzerland and within the larger geological context of the Aar massif.

interpreted to be indicative for diffusive He-loss owing to deformation-induced crystal defects (Whipp and Ehlers, 2007; Gorynski et al., 2014) or (ii) older, indicating possible He gain (Milesi et al., 2019, 2020).

Since apatite is prone to dissolution under acidic conditions (e.g. during diagenesis or hydrothermal activity) and can recrystallize from such hydrothermal fluids in a later stage, interpretation of apatite low-temperature chronometric data can be complex (e.g. Egli et al., 2018a; Milesi et al., 2020). Therefore, a better understanding on how to distinguish neo- or recrystallised apatite is needed. Promising approaches to identify re-crystallised apatite include striking difference in chemical trace element composition (e.g. Harlov, 2015), or by apatite U/Pb isotope ages (e.g., Henrichs et al., 2018, 2019). The application of such approaches, however, can be hampered by (i) small apatite grain

size and/or (ii) the often isolated occurrence of grains.

This study addresses how low-temperature chronometry and their resetting mechanisms (diffusional loss and/or recrystallization) can be affected by hydrothermal activity and thus can inform and constrain the temporal continuity and maximum temperature of hydrothermal activity. We used detailed apatite microstructure analysis and trace-element measurements from the Grimsel Breccia Fault, a long-lived fault-bound hydrothermal zone within the Aar massif (central Swiss Alps, (Belgrano et al., 2016)). The Grimsel Breccia Fault shows present-day subthermal water effluence, which may not reset the AHe system at present-day subsurface levels. However, these measured near-surface temperatures are related to mixing of an uprising hotter water with infiltrating cold surface water (Waber et al., 2017). The exact depth where this mixing

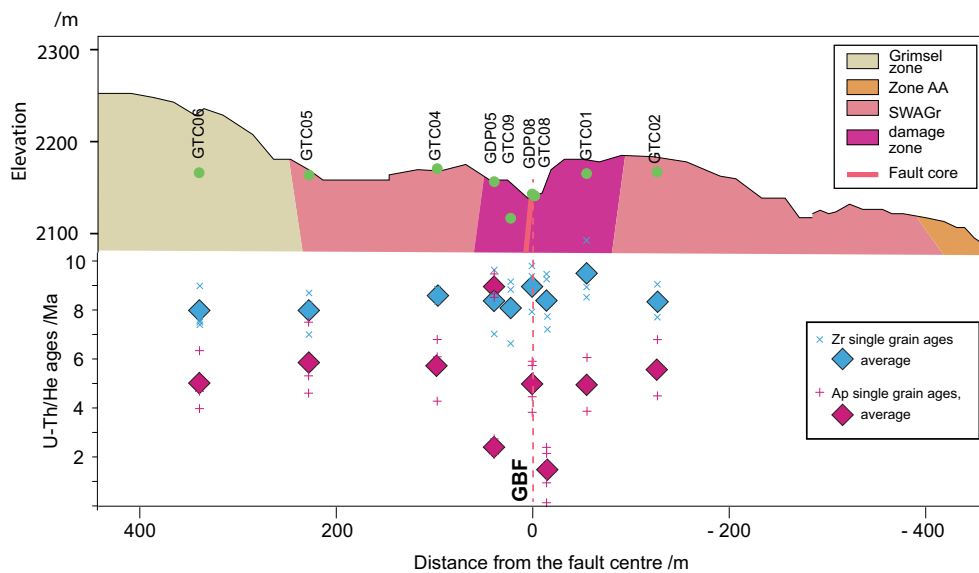


**Fig. 2.** Top part: Geological transect (see Fig. 1 for location) with the projected sample locations/names and bedrock litho-tectonic units (GBF = Grimsel breccia fault). Bottom part: average and single-grain AHe and ZHe ages of the samples (see Tables 1, 2 and 3). The analytical errors on single-grain ages and the  $1\sigma$  uncertainties on pooled-average ages are smaller than symbol sizes.

process occurs is unknown. Thermal modelling, fluid-inclusion data, and present-day fluid isotopic compositions demonstrate upwelling of deeper hot water ( $<100\text{ }^{\circ}\text{C}$ ) over long periods (Waber et al., 2017; Diamond et al., 2018). Using AHe and ZHe age transects collected from host granites across tectonites of the Grimsel Breccia Fault, we aim to investigate the impact of known thermal/hydrothermal perturbations on low-temperature chronometry data.

## 2. Geological setting

The study area is situated in the southern part of the central Aar Massif in Switzerland (Figs. 1 and 2). The Aar Massif consists of pre-Variscan basement ortho- and paragneisses intruded by late- to post-Variscan granitoid intrusions (e.g. Abrecht, 1994; Berger et al., 2017), locally overlain by late Paleozoic sediments. The area is characterized by a dominantly ENE-WSW striking network of shear zones (Wehrens et al., 2016, 2017), initialised during metamorphism as ductile reverse faults. Strain partitioning led to the reactivation of reverse faults as dextral oblique to strike-slip faults since ca. 14–12 Ma (Rolland et al., 2009; Wehrens et al., 2017). With progressive strike-slip shearing and cooling, the rheology changed towards a brittle deformation style. Structurally, brittle deformation localizes along some of the major shear zones and develops fault linkages forming the fault network of the Grimsel Breccia Fault (Belgrano et al., 2016). This fault zone consists of breccias, cataclastites and fault gouges as well as 10–20 m wide fractured damage zones at the transition between host rocks and fault cores (Fig. 3; Belgrano et al., 2016). The related fossil hydrothermal system is well documented by hydrothermal minerals and has been dated to be active since at least 3.3 Ma (Ar/Ar dating on hydrothermal adularia; Hofmann et al., 2004). The maximum temperature of the hydrothermal system is supposed to be of the order of the calculated primary fluid temperatures (i.e.  $>165\text{ }^{\circ}\text{C}$ ), based on fluid chemical composition (Waber et al., 2017; Diamond et al., 2018; Wanner et al., 2019). The lateral extent of hydrothermal water infiltration during the activity of the fossil system is estimated based on mapped mineralization, which occurs in patches around a central breccia zone and reaches up to a few hundreds of meters into the host rock (Belgrano et al., 2016).

Present-day waters collected at 1900 m a.s.l. along the TransitGas tunnel indicate temperatures of  $50 \pm 10\text{ }^{\circ}\text{C}$  for the deep hydrothermal proportion of the present-day discharging hydrothermal fluid (Waber

et al., 2017; Diamond et al., 2018; Wanner et al., 2019) that is mixed with cooler water fractions. This mixing results in an outflow temperature of  $22\text{--}28\text{ }^{\circ}\text{C}$  (Pfeifer et al., 1992; Sonney and Vuataz, 2008; Waber et al., 2017). Note that the depth region of mixing between warm hydrothermal and cold meteoric waters has remained unknown to date. Stable-isotope data of present-day waters indicate an infiltration age of the deep geothermal water of as old as 30 ka, suggesting long residence times in the system (Waber et al., 2017). The water temperatures are of the order of  $110\text{--}120\text{ }^{\circ}\text{C}$  at depth (Waber et al., 2017; Diamond et al., 2018; Wanner et al., 2019). Recent analysis of paleo-earthquake proxies suggests stages of fault healing and rupturing at seismic rates (Berger and Herwegh, 2019). This information, combined with ongoing background regional seismic activity and discharge of hot water, suggests an episodically recurring hydrothermal activity since at least 3.3 Ma. Whether the system remained continuously active during this entire period represents an open question.

## 3. Sample materials and methods

The Grimsel Breccia Fault contains a brittle fault core consisting of breccias, cataclastites and fault gouges (Hofmann et al., 2004; Belgrano et al., 2016) enveloped by a 10–20-m wide fractured damage zone. The breccias themselves can also be differentiated into a general group of angular not sorted clasts of older cataclastites/country rocks alternating with a cockade bearing breccia (Berger and Herwegh, 2019). Note that among all fault-related tectonites the latter show the highest porosities and permeability (Egli et al., 2018b). The directly adjacent country rock is a metagranite of the SW Aar granite bounded to the north by polymetamorphic gneisses. The granite shows a relatively weak foliation, barely distinguishable in hand samples. However, the SW Aar granite locally concentrates late-stage fractures in the vicinity of the Grimsel Breccia Fault. We investigated 8 bedrock samples. Samples GTC01, –02, –04 and –05 are from the SW Aar granite and sample GTC06 is from the polymetamorphic gneisses (Figs. 1 and 2; Table 1). Inside the Grimsel Breccia Fault, samples were taken from breccias and cataclastites at the surface and from a drill-hole (samples GDP05, GDP08 and GTC08; Figs. 1–3).

Samples collected from host granites across tectonites of the Grimsel Breccia Fault were comminuted using the SelFrag at the University of Bern and sieved to a fraction of 63–250  $\mu\text{m}$ ; heavy minerals were

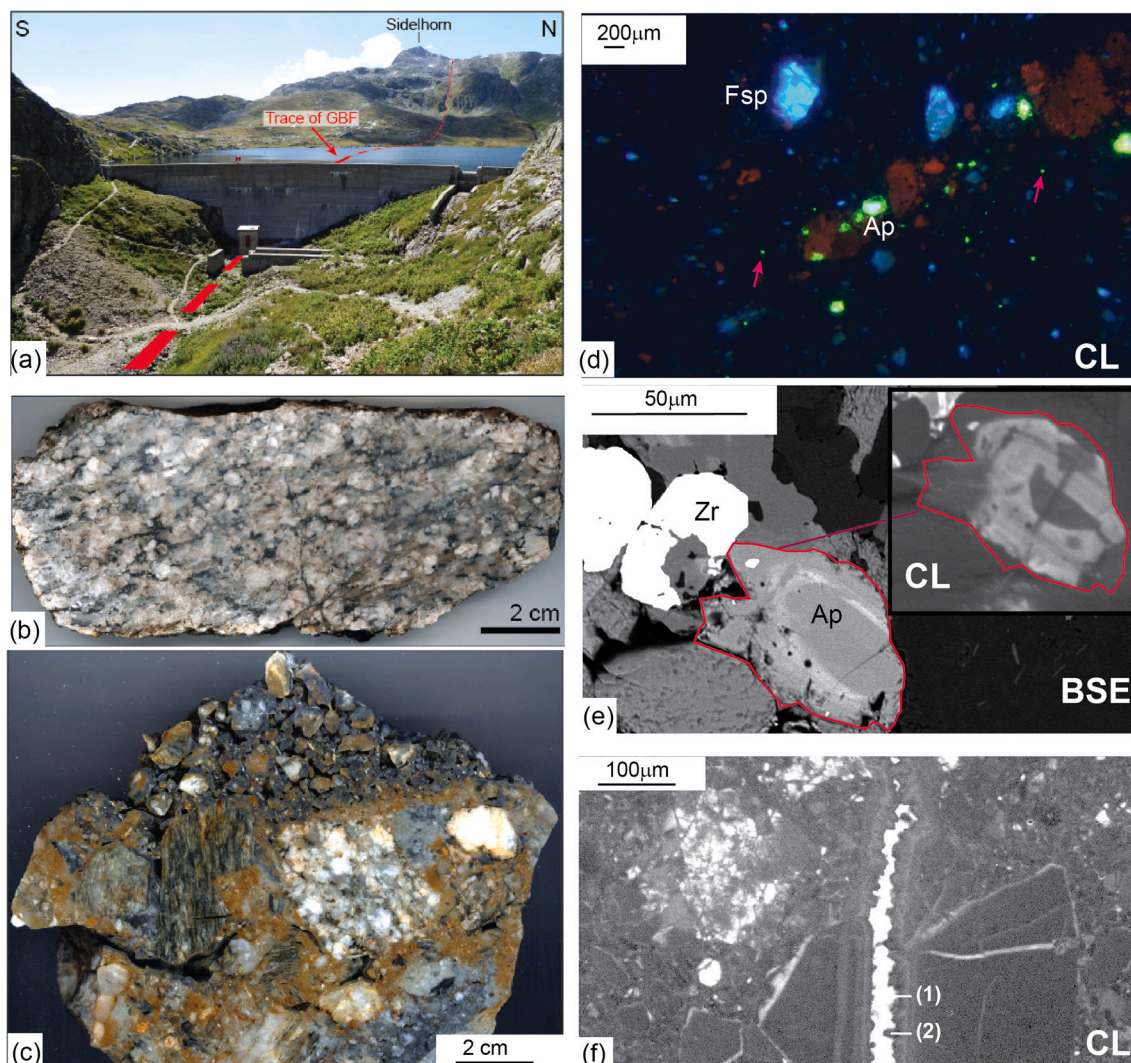


**Fig. 3.** a) View westward along the Grimsel Breccia Fault. The morphological incision follows the hydrothermally mineralized/brecciated center of the fault. Viewpoint: location of the drill-hole (Egli et al., 2018a, 2018b). b) Hand specimen of sample GTC02 showing moderately-sheared SW Aare granite. c) Typical hand specimen of fossil hydrothermal breccia displaying open space between clasts. Samples GBP08 & GTC08 had the same appearance. d) Optical CL-image of a SW Aare granite sample. The green luminescing minerals are apatite (Ap), close to feldspars (Fsp). Note the presence of small apatite crystals (see pink arrows for locations). e) BSE image showing a low-deformed Aare Granite with zircon (Zr) and apatite (Ap). Note the zonation in apatite already visible in backscatter electrons (BSE). Small inset: same apatite grain as CL image (SEM). f) CL image (SEM) from a breccia with an open fracture (bright luminescing area, caused by glue), showing newly-growing minerals (2) into the open space (1). (For interpretation of the references to colour in this figure legend, the reader is referred to the web version of this article.)

separated using a magnetic separator and heavy liquids. After washing and drying, zircon and apatite grains were hand-picked from the remaining grain separates under a standard binocular microscope to obtain 4–5 inclusion-free grains of suitable size for each sample. The apatite grains generally showed small grainsize (<100  $\mu\text{m}$ ), hypidiomorphic shapes with broken-off tips and a gnarled surface (Fig. 4a). Despite the abundance of inclusions and micro-cracks, suitable inclusion- and crack-free grains could be selected for all samples. The zircon grains were relatively large (80–100  $\mu\text{m}$  wide, 200–300  $\mu\text{m}$  long) and mostly idiomorphic in shape, which allowed for a careful selection of macroscopically largely inclusion-free grains. Most of the zircons retained their idiomorphic shape despite the partly intense deformation (e.g. brecciation), but very often they showed many inclusions (Fig. 4b). U, Th, Sm and He measurements were performed at the University of Tübingen. Analytical details are given in Appendix 1, which also explains the procedures for age calculations and error propagation.

Furthermore, additional apatite grains were embedded in epoxy resin for some key samples. These aliquots were polished to investigate

the internal grain microstructures (Fig. 4) using the Cathodoluminescence (CL) signal on a ZEISS EVO 50 scanning electron microscope (University of Bern). Texturally-controlled trace-element concentrations in these grains were measured with a LA-ICP-MS at the University of Bern. The LA-ICP-MS analytical procedure is documented in detail in Appendix 2.

## 4. Results

### 4.1. (U-Th)/He data

Independent of the bedrock structure, the ZHe age pattern is consistent with average ZHe between  $8.0 \pm 0.2$  and  $9.5 \pm 0.5$  Ma (Tables 1, 2 and 3; Appendix 1). In contrast, the apatite samples show a larger spread in single-grain and average AHe ages. The host rock samples farthest away from the hydrothermal zone (i.e. GTC01, -02, -04, -05 and -06) show relatively consistent average AHe ages of between  $4.9 \pm 0.4$  and  $5.8 \pm 0.2$  Ma, with a single-grain AHe spread of  $\sim 2$  Ma

**Table 1**Summary of the sample location and available age data. For detail data of this study see [Tables 2 and 3](#) and [Appendix 1](#).

Sample	Ar-ages [Ma]	ZFT [Ma]	ZHe [Ma]	AFT [Ma]	AHe [Ma]	Longitude	Latitude	Elevation	distance to GBF [m]	$\Delta h$ [m]	Ref
AV45				6.9	5.2	8.28638	46.66772	1505	12,700	-650	V09
AV83				7.9		8.33535	46.56727	2005	1000	-150	V09
KAW2213	15.1 <sup>(1)</sup>	12.4		5.3		8.3333	46.5592	2160	715	0	MS90; D86
GTC06			8.0		5.0	8.34083	46.56296	2167	135	0	this study
GTC05			8.0		5.8	8.34392	46.56244	2166	92	0	this study
GTC04			8.6		5.8	8.34423	46.5616	2170	40	0	this study
GDP05 (i)			8.4		9.0	8.34468	46.56088	2160	15	0	this study
(ii)					2.4						
S70	12.8 <sup>(2)</sup>					8.3275	46.5545	2275	0	100	R09
GR23	3.3 <sup>(3)</sup>					8.3085	46.5539	2630	0	500	H04
GTC08			8.4		1.5	8.34496	46.56054	2145	0	0	this study
GDP08			9.0		5.4	8.34496	46.56054	2145	0	0	this study
GTC01			9.5		4.9	8.3459	46.56035	2164	-22	0	this study
GTC02			8.3		5.6	8.3459	46.56001	2175	-51	0	this study
AV95				7.1		8.35709	46.5608	1790	-380	-350	V09
KAW96				4.8		8.3563	46.5392	1610	-1700	-500	W77
AV101				4.6		8.35443	46.53833	1405	-2550	-750	V09

(1) K/Ar age from white mica mineral separate of gneiss; (2) Ar/Ar ages on white micas from mylonites, which are the precursor of the GBF; (3) Ar/Ar age of a hydrothermal adular from the GBF.

$\Delta h$  are summarized in 50 m intervals. Data from: V09: [Vernon et al., 2009](#); MS90: [Michalski and Soom, 1990](#); D86: [Dempster, 1986](#); R09: [Rolland et al., 2009](#); W77: [Wagner et al., 1977](#); H04: [Hofmann et al., 2004](#).

([Tables 1 and 2](#); [Appendix 1](#); [Fig. 2](#)). Interestingly, sample GDP08 from the hydrothermal breccia also lies within this trend ( $5.4 \pm 0.2$  Ma). The second sample from the hydrothermal breccia (GTC08) yields younger ages, with average AHe age of  $1.5 \pm 0.5$  Ma and single-grain AHe ages as low as 0.2 Ma. In contrast, sample GDP05 (also from the breccia) shows high dispersion in single-grain AHe ages, with 2 age clusters at  $9.0 \pm 0.4$  and  $2.4 \pm 0.1$  Ma. Single-grain AHe ages in all samples show significant variability; however, no relationship to eU (effective uranium content) or grain size is obvious ([Fig. 5](#)). The absence of such relationships may indicate that a process different from He diffusion kinetics is responsible for the observed spread in apatite single-grain (U-Th)/He ages.

In summary, ZHe ages show constant values between 7.96 and 9.51 Ma for the average ages and relative constant values for the relevant ZHe single grain ages ([Table 3](#)). Contrasting the expected and constant ZHe ages, the AHe ages show a very narrow zone of substantial age variations within a few tens of meters of the Grimsel Breccia Fault ([Fig. 2](#); [Table 3](#)).

#### 4.2. Apatite microstructure

Apatite microstructures in host rocks, including the Grimsel Breccia Fault zone, indicate the occurrence of different processes leading often to grain size reduction ([Fig. 3](#)). On one hand, the grain size reduction may be caused by fracturing ([Fig. 4](#)). On the other hand, small grains (<5  $\mu\text{m}$ ) with roundish shapes are frequent, which most likely present recrystallization of hydrothermal apatite ([Fig. 3](#)). Unfortunately, the small grain sizes prevent isotope or trace element measurements for these grains. The breccia samples themselves have to be subdivided into clasts and matrix. The clasts preserve the primary gneissic texture, their grain size and primary mineralogy. In contrast, the matrix is dominated by evidence for frictional deformation and hydrothermal processes ([Fig. 3c + f](#)). Inside the clasts, primary apatites are frequent. These apatites are shielded from further deformation and/or re-precipitation processes, hence their potential AHe resetting should be dominated by diffusion processes. The hydrothermal processes led to growth of new minerals as for example Mn-oxides, quartz, celadonite ([Hofmann et al., 2004](#)) and possibly also apatites. The size of such newly formed apatites may vary between a few micron- to hundreds of microns.

#### 4.3. Apatite composition

Separated apatite grains (e.g. sample GDP08) with apparent non-reset AHe ages typically show magmatic growth zonation ([Figs. 3 and 4b](#)). In contrast, in samples where apatite yields significantly younger

AHe ages (GTC08), those apatites are homogeneous under CL and no internal grain structures are detected ([Fig. 4g, h](#)). In addition, apatite grains of sample GTC02 show thin dark rims on bright cores ([Fig. 4c, d](#)). The overgrowth parts and the homogeneous grains in sample GTC08 have similar CL characteristics (i.e. CL-intensity). An illustrating example in [Figs. 3e and 4e](#) shows grains with characteristic magmatic growth zonation. Interestingly, these variations in CL-signal correspond to observed variations in measured trace elements. The REE patterns change fundamentally between apatite core and rim domains. Apatite cores show light REE enriched patterns, as is typical for granites ([Fig. 6](#); [Belousova et al., 2002](#); [Dempster et al., 2003](#); [O'Sullivan and Chew, 2020](#); [O'Sullivan et al., 2020](#)), which are labelled as Group 1. Group 2 apatite rims and individual grains ([Fig. 4](#)) have HREE enriched REE element patterns ([Fig. 6](#)).

In addition, the bulk concentrations of REE + Y for Group 2 are significantly lower than those of Group 1 ([Fig. 6](#)). For example, Group 1 analysis shows Ce concentrations between 600 and 2200 ppm, whereas the Group 2 samples have Ce concentrations in the range of 0.4–1.3 ppm. In addition, the Sr concentrations are slightly higher in Group 2 (up to 1700 ppm) compared to Group 1 apatite (~170 - ~600 ppm; [Fig. 6](#), [Appendix 2](#)). Group 2 apatite grains are characterized by low Sm concentrations and rejuvenated young AHe ages ([Fig. 6](#)).

#### 4.4. Thermal modelling

We used the software “HeFTy” ([Ketchum, 2005](#)) to evaluate apatite response to a rather constant regional cooling history affected by (short) fluid-mediated heat pulses on AHe ages, as may be expected by a temporarily variable hydrothermal activity during fluid pulses. In the following, two effects are inspected by the thermal modelling approach based on He diffusion in apatites: (1) different duration ( $=\Delta t$ ) of heating, and (2) different temperature anomaly ( $=\Delta T$ ) caused by hydrothermal fluid flow. The modelling approach assumes variably hot temperature fluid influx at the time when the host rocks are located at 28 °C, which has been read out by the cooling path outside the fault zone at 2 Ma (see background cooling path calculated and shown in [Fig. 7a](#)). The reasoning for position of re-heating from hydrothermal activity is based on the inverse background model using the data of sample GTC06 (sample outside the Grimsel Breccia Fault, [Fig. 7a](#)). Using lower  $\Delta T$  anomalies of up to +40 °C over durations up to Ma timescales (path 1 and 2) to the background path has a minor effect on modelled AHe ages. Our modelling reveals a nearly complete AHe resetting for  $\Delta T$  of +60 °C ( $T_{\text{max}} = 88$  °C) when the local hydrothermal fluid flux is active over a



**Table 2**  
Apatite U- Th/He results.

Sample	U238_mol	U235_mol	Th232_mol	Sm147_mol	Raw age (Ma)	Raw age_SD (Ma)	FT	Corrected age (Ma)	Corrected age SD (Ma)
Ap_GDP05-Ap3	1.54E-13	1.13E-15	4.10E-13	5.68E-14	6.26	0.18	0.726	8.63	0.25
Ap_GDP05-Ap5	1.13E-13	8.32E-16	1.71E-13	2.37E-14	5.8	0.3	0.674	8.66	0.52
Ap_GDP05-Ap6	1.40E-13	1.03E-15	3.73E-13	5.16E-14	5.8	0.2	0.602	9.59	0.39
<b>Ap GDP05 (I)</b>								<b>8.96</b>	<b>0.39</b>
Ap_GDP05-Ap2	1.79E-13	1.31E-15	5.11E-13	7.06E-14	1.88	0.06	0.686	2.75	0.08
Ap_GDP05-Ap4	1.21E-13	8.92E-16	2.59E-13	3.58E-14	1.44	0.05	0.682	2.12	0.07
<b>Ap GDP05 (II)</b>								<b>2.43</b>	<b>0.08</b>
Ap_GDP08-Ap1	4.07E-13	2.99E-15	6.95E-13	9.61E-14	4.27	0.12	0.739	5.78	0.17
Ap_GDP08-Ap2	3.63E-13	2.67E-15	4.53E-13	6.27E-14	2.84	0.11	0.733	3.88	0.15
Ap_GDP08-Ap3	1.36E-13	1.00E-15	3.78E-15	5.22E-16	4.14	0.15	0.700	5.91	0.22
Ap_GDP08-Ap4	3.42E-13	2.52E-15	4.80E-13	6.63E-14	2.68	0.07	0.596	4.49	0.12
Ap_GDP08-Ap5	1.05E-13	7.73E-16	2.55E-13	3.53E-14	3.03	0.09	0.444	6.82	0.21
<b>Ap GDP 08</b>								<b>5.37</b>	<b>0.17</b>
Ap_GTC01-Ap1	5.55E-14	4.08E-16	1.02E-13	1.41E-14	2.6	0.2	0.671	3.87	0.26
Ap_GTC01-Ap2	1.31E-13	9.60E-16	1.86E-13	2.57E-14	6.8	0.3	0.647	10.45	0.39
Ap_GTC01-Ap3	8.85E-14	6.50E-16	7.17E-14	9.92E-15	3.6	0.3	0.593	6.07	0.55
Ap_GTC01-Ap4	9.24E-14	6.79E-16	1.79E-13	2.48E-14	3.0	0.2	0.629	4.83	0.32
<b>Ap GTC01</b>								<b>4.92</b>	<b>0.38</b>
Ap_GTC02-Ap1	1.53E-13	1.12E-15	2.60E-13	3.59E-14	23.7	1.0	0.649	36.55	1.59
Ap_GTC02-Ap2	1.18E-13	8.69E-16	1.45E-13	2.01E-14	17.8	0.8	0.645	27.58	1.19
Ap_GTC02-Ap3	1.12E-13	8.24E-16	2.04E-13	2.82E-14	2.8	0.1	0.629	4.50	0.19
Ap_GTC02-Ap4	2.91E-13	2.14E-15	3.87E-13	5.36E-14	5.2	0.2	0.771	6.77	0.22
<b>Ap GTC02</b>								<b>5.63</b>	<b>0.20</b>
Ap_GTC04-Ap1	6.62E-14	4.86E-16	1.38E-13	1.91E-14	17.06	0.60	0.651	26.19	0.92
Ap_GTC04-Ap2	9.24E-14	6.79E-16	1.37E-13	1.89E-14	4.78	0.21	0.703	6.79	0.30
Ap_GTC04-Ap3	1.82E-13	1.34E-15	3.31E-13	4.58E-14	3.96	0.10	0.644	6.14	0.16
Ap_GTC04-Ap5	1.86E-13	1.37E-15	3.33E-13	4.61E-14	2.88	0.08	0.666	4.32	0.11
<b>Ap GTC04</b>								<b>5.75</b>	<b>0.19</b>
Ap_GTC05-Ap1	1.13E-13	8.30E-16	3.23E-13	4.47E-14	3.05	0.08	0.657	4.64	0.13
Ap_GTC05-Ap2	7.45E-14	5.47E-16	2.27E-13	3.13E-14	9.02	0.27	0.682	13.23	0.40
Ap_GTC05-Ap3	8.40E-14	6.17E-16	2.48E-13	3.44E-14	4.75	0.13	0.630	7.53	0.21
Ap_GTC05-Ap4	9.81E-14	7.21E-16	2.72E-13	3.76E-14	3.91	0.12	0.739	5.29	0.17
<b>Ap GTC05</b>								<b>5.82</b>	<b>0.17</b>
Ap_GTC06-Ap1	9.18E-14	6.74E-16	1.18E-13	1.64E-14	2.88	0.11	0.716	4.02	0.16
Ap_GTC06-Ap2	8.40E-14	6.17E-16	9.78E-14	1.35E-14	4.00	0.15	0.628	6.37	0.24
Ap_GTC06-Ap4	1.62E-13	1.19E-15	1.83E-13	2.53E-14	2.88	0.10	0.615	4.69	0.16
<b>Ap GTC06</b>								<b>5.03</b>	<b>0.19</b>
Ap_GTC08-Ap1	1.88E-14	1.38E-16	3.78E-15	5.22E-16	1.4	0.4	0.825	1.71	0.44
Ap_GTC08-Ap2	6.47E-14	4.75E-16	1.23E-15	1.70E-16	0.1	0.1	0.709	0.18	0.09
Ap_GTC08-Ap3	6.21E-14	4.56E-16	1.60E-15	2.22E-16	1.8	0.2	0.817	2.15	0.23
Ap_GTC08-Ap4	1.12E-14	8.22E-17	7.51E-16	1.04E-16	1.7	0.6	0.716	2.40	0.82
Ap_GTC08-Ap5	8.55E-15	6.28E-17	2.89E-15	4.00E-16	0.5	0.5	0.532	0.98	0.95
<b>Ap GTC08</b>								<b>1.48</b>	<b>0.51</b>

relatively long time interval (>1 Ma; path 3 in Fig. 7). Alternative to such long durations, a heating interval of 10–100 ka with a larger  $\Delta T$  of +110 °C ( $T_{max} = 138$  °C, see Wanner et al. (2019) and Waber et al. (2017) for temperature estimates in the Grimsel Breccia Fault) is sufficient to influence AHe ages substantially (path 4 in Fig. 7c).

## 5. Discussion

CL-images, trace element concentration data and AHe ages reveal two groups of apatite. A first group is characterized by primary growth zonation (visible in CL-images), a flat REE pattern and consistent AHe ages that fit the regional cooling trend (see also Table 1). Mineral zonation in apatite are typical magmatic features as known from granitic host rocks (e.g., Dempster et al., 2003). In addition, this apatite group has bulk REE concentrations ~1000 times higher than chondritic values. Thus, Group 1 apatite is best described as thermochronometer. The second group is characterized by absence or weak zonation, HREE-enriched REE pattern with partially subchondritic LREE concentrations and rejuvenated AHe ages. The bulk REE concentrations of apatite from Group 2 are only ~10 times higher than chondritic values. Such prominent differences in trace element concentrations and signatures are impossible to result from diffusional processes and, together with significantly younger AHe ages, do require re-crystallization. These grains and associated AHe ages therefore record re-crystallization processes and therefore need to be interpreted as geochronometers.

### 5.1. Linking AHe ages with the geological context

The above-mentioned Group 1 apatites present AHe ages that record the regional evolution of rock cooling and exhumation. Furthermore, all ZHe ages of this study are interpreted as a record of the regional cooling and exhumation history, given agreement with data within the Aar massif (Nibourel et al., 2021) and no perturbation along the investigated transect (Fig. 2). Combining our AHe - ZHe results with literature thermochronometric data and proposed closure temperatures of these systems, we derived a regional cooling history for the Grimsel area (Fig. 8; Michalski and Soom, 1990; Vernon et al., 2009; Glotzbach et al., 2010; Valla et al., 2012, 2016; Herwegh et al., 2020). In contrast, ages of minerals precipitated in fractures/clefts may date hydrothermal fluid activity. One example is newly-grown adularia (fluid inclusion microthermometric data; Nr. 2 in Fig. 8; Hofmann et al., 2004; Nr. 4 in Fig. 8; Rossi and Rolland, 2014). Using the Th/Pb system, precipitation age and temperature estimates also exist for cleft monazites (Nr. 3 in Fig. 8, Bergemann et al., 2017; Appendix 3). The young AHe ages of the above-reported newly-grown apatites (Group 2 AHe ages) may also record the time of hydrothermal mineral growth (Nr. 1 in Fig. 8; see detailed discussion in Sections 5.2, 5.3 and 5.4). In any case, the obtained AHe age should be close to when the system reached the AHe closure temperature in the Grimsel Breccia Fault branch being hydrothermally active at that time.

Independent of absolute data, the occurrence indicating different

Table 3

Zircon U-Th/He data.

Sample	U238_mol	U235_mol	Th232_mol	Raw age (Ma)	SD (Ma)	FT	Corrected age (Ma)	Corrected SD (Ma)
Zr_GDP05-Zr1	2.67E-12	1.96E-14	1.76E-12	6.8	0.2	0.700	9.66	0.24
Zr_GDP05-Zr2	3.17E-12	2.33E-14	1.43E-12	10.0	0.2	0.582	17.22	0.42
Zr_GDP05-Zr3	1.29E-11	9.45E-14	3.83E-12	6.0	0.1	0.724	8.36	0.19
Zr_GDP05-Zr4	2.63E-11	1.93E-13	7.12E-12	4.8	0.1	0.675	7.06	0.15
<b>Zr GDP05</b>							<b>8.36</b>	<b>0.19</b>
Zr_GDP08-Zr1	3.53E-11	2.60E-13	3.91E-12	7.5	0.2	0.794	9.39	0.24
Zr_GDP08-Zr2	9.38E-12	6.89E-14	3.42E-13	6.3	0.1	0.789	7.93	0.19
Zr_GDP08-Zr3	1.01E-11	7.42E-14	2.30E-12	7.2	0.2	0.816	8.83	0.27
Zr_GDP08-Zr4	4.33E-12	3.18E-14	1.35E-12	6.6	0.2	0.675	9.80	0.26
Zr_GDP08-Zr5	2.11E-11	1.55E-13	1.08E-11	6.7	0.2	0.756	8.88	0.26
<b>Zr GDP08</b>							<b>8.97</b>	<b>0.24</b>
Zr_GTC01-Zr1	2.10E-10	1.54E-12	3.63E-11	7.2	0.3	0.851	8.51	0.35
Zr_GTC01-Zr2	5.12E-12	3.76E-14	1.63E-12	6.2	0.4	0.699	8.94	0.63
Zr_GTC01-Zr3	4.22E-11	3.10E-13	1.25E-11	8.7	0.6	0.804	10.84	0.70
Zr_GTC01-Zr4	3.28E-11	2.41E-13	9.87E-12	7.3	0.3	0.745	9.76	0.40
<b>Zr GTC01</b>							<b>9.51</b>	<b>0.52</b>
Zr_GTC02-Zr2	8.47E-12	6.22E-14	3.81E-12	5.4	0.3	0.705	7.69	0.45
Zr_GTC02-Zr3	2.96E-11	2.18E-13	8.46E-12	6.8	0.7	0.825	8.22	0.80
Zr_GTC02-Zr4	1.64E-11	1.21E-13	6.16E-12	6.7	0.4	0.739	9.03	0.52
<b>Zr GTC02</b>							<b>8.31</b>	<b>0.59</b>
Zr_GTC04-Zr1	2.02E-11	1.49E-13	4.34E-12	13.8	0.2	0.744	18.52	0.30
Zr_GTC04-Zr2	1.41E-11	1.04E-13	4.01E-12	6.0	0.1	0.720	8.39	0.21
Zr_GTC04-Zr3	4.80E-12	3.52E-14	1.53E-12	5.7	0.2	0.651	8.81	0.26
Zr_GTC04-Zr4	1.01E-11	7.38E-14	3.12E-12	6.5	0.1	0.752	8.65	0.18
<b>Zr GTC04</b>							<b>8.62</b>	<b>0.21</b>
Zr_GTC05-Zr1	3.16E-11	2.32E-13	1.14E-11	6.2	0.2	0.760	8.22	0.21
Zr_GTC05-Zr2	3.24E-11	2.38E-13	1.19E-11	5.4	0.1	0.775	6.98	0.16
Zr_GTC05-Zr3	8.89E-12	6.53E-14	3.63E-12	5.7	0.1	0.659	8.67	0.21
Zr_GTC05-Zr4	9.35E-12	6.87E-14	3.94E-12	5.4	0.1	0.665	8.17	0.14
<b>Zr GTC05</b>							<b>8.01</b>	<b>0.18</b>
Zr_GTC06-Zr1	4.27E-11	3.14E-13	1.05E-11	6.8	0.2	0.760	8.99	0.27
Zr_GTC06-Zr2	1.32E-11	9.67E-14	4.71E-12	5.7	0.2	0.718	7.94	0.22
Zr_GTC06-Zr3	8.93E-12	6.56E-14	3.06E-12	5.1	0.1	0.684	7.43	0.19
Zr_GTC06-Zr4	1.40E-11	1.03E-13	4.04E-12	5.3	0.1	0.705	7.48	0.20
<b>Zr GTC06</b>							<b>7.96</b>	<b>0.22</b>
Zr_GTC08-Zr1	7.21E-12	5.29E-14	2.87E-12	6.1	0.4	0.661	9.28	0.58
Zr_GTC08-Zr2	8.46E-12	6.21E-14	2.33E-12	5.3	0.2	0.731	7.22	0.34
Zr_GTC08-Zr3	4.95E-12	3.64E-14	1.50E-12	5.4	0.2	0.697	7.72	0.32
Zr_GTC08-Zr4	1.93E-11	1.42E-13	6.01E-12	6.8	0.2	0.721	9.42	0.34
<b>Zr GTC08</b>							<b>8.41</b>	<b>0.40</b>
Zr_GTC09-Zr1	2.16E-11	1.59E-13	1.07E-11	5.3	0.3	0.677	7.89	0.47
Zr_GTC09-Zr2	1.94E-11	1.42E-13	5.09E-12	6.1	0.3	0.686	8.85	0.40
Zr_GTC09-Zr3	1.92E-11	1.41E-13	6.86E-12	6.4	0.3	0.694	9.16	0.45
Zr_GTC09-Zr4	4.07E-11	2.99E-13	3.19E-12	4.9	0.2	0.734	6.66	0.30
<b>Zr GTC09</b>							<b>8.14</b>	<b>0.40</b>

temperatures at the same time (compare yellow trend against blue arrows in Fig. 8) supports the findings of Janots et al. (2019), who reported different T-t data in clefts compared to their country rocks. The prerequisite for data recording a locally variable temperature at similar times is the occurrence of sufficient and fast enough fluid flow to allow mineral precipitation. These factors require a certain permeability of such zones, which is the common ground of the cleft example of Janots et al. (2019) and the reported Grimsel Breccia Fault. In this context, it is important to note that the scale of such thermal perturbations could be relatively small (Fig. 2; see also Janots et al., 2019) or could occur at larger scale within the Aar massif (e.g. Valla et al., 2016).

### 5.2. Discussing the thermal model results with possible resetting mechanisms

In order to constrain this different apatite behaviour (diffusion and/or re-crystallization), we have estimated the upper bounds of the diffusional impact in terms of temperature and time in Section 4.4. The main result of the diffusional modelling is that either very high local temperatures (+110 °C) over a ka time scale or moderate heat input (+60 °C) over Ma time scales is required to reset the AHe system (Fig. 7, Section 4.4). Both scenarios for possible diffusional AHe resetting are unlikely as: (1) large differences between “cold” host rock and spatially-

restricted fault-bound hot hydrothermal fluid flow will cool the fluids rapidly (in addition, boiling of aqueous fluids is likely along such paths); (2) long-term fluid flow will heat the country rock substantially (see model of Wanner et al., 2019; next paragraph), which we do neither see in the ZHe nor in the AHe data (Fig. 2).

Besides such estimates, the understanding of the thermal history in small-scale hydrothermal zones requires at least a 2D hydro-thermal model, which includes both fluid flow dynamics and the thermal evolution of the country rocks. Wanner et al. (2019) calculated such a model assuming the 3D evolution of a steady-state thermo-hydraulic system. Their modelling results indicate the presence of a km-wide zone of elevated temperature of the rock body at thermal steady state, which is spatially relatively stable and distributed around the hydrothermal fault. However, the missing complete AHe resetting of all our apatite samples at the inferred fluid temperatures over the last 3 Ma (Waber et al., 2017) argues against a long-lasting (Ma timescales) hydrothermal structure producing a steady-state positive thermal anomaly (see next section). This situation would require a complete diffusional resetting of the apatite system.

### 5.3. The AHe chronometer in hydrothermal systems

The Grimsel Breccia Fault provides evidence that all three scenarios

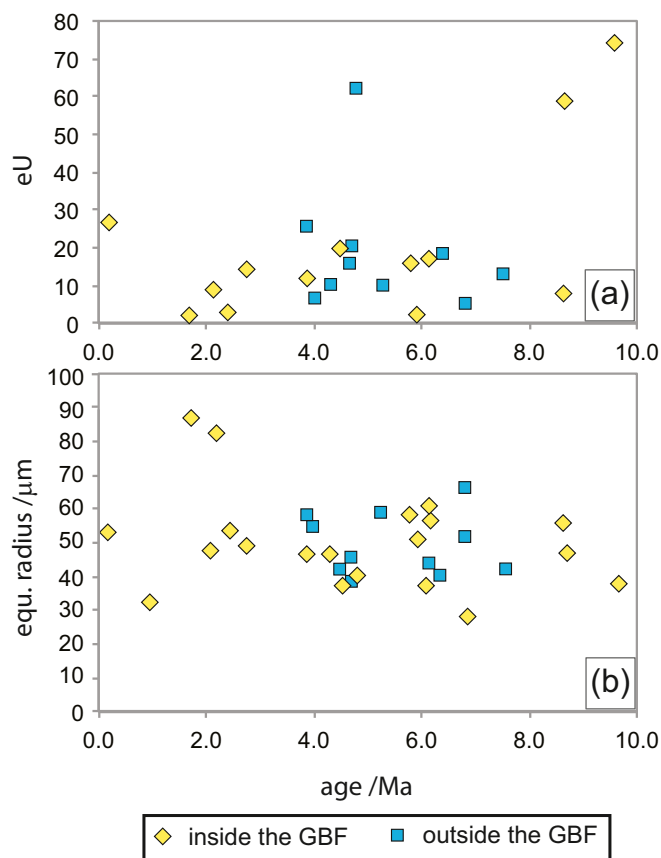


**Fig. 5.** (a) Plot showing the effective uranium content (eU) versus the single-grain apatite (U-Th)/He ages. (b) Plot showing the sphere-equivalent radius (SER) versus single-grain apatite (U-Th)/He ages. Note the non-existing correlation for samples from the Grimsel Breccia Fault (GBF) as well as samples outside the fault in both plots.

affecting AHe ages as reported in the literature (Milesi et al., 2019, 2020) occurred at this site:

- 1) AHe ages from the country rocks preserve the regional cooling trend (Group 1);
- 2) Old AHe ages occur, which apparently are too old compared to the regional cooling (sample GDP05, Fig. 2);
- 3) AHe ages which are significantly younger as the regional trend by newly-formed (re-crystallization) crystals (Group 2).

Importantly, our data provide evidence for (re-)crystallization of apatite grains displaying a very distinct chemical composition (Group 2, Fig. 6). Combining this information with a 3D thermal modelling (Wanner et al., 2019) indicates that the hydrothermal AHe system is not in a regional thermal steady state, requiring a more complex system with spatial and temporal variability of the local thermal structure.

The very localized abrupt fault-bound variation in AHe ages compared to the regional background trend suggests occurrence of localized as well as episodically-active fluid pathways, out of thermal equilibrium with enclosing rocks. Such temporal variations of small-scale fluid flow are consistent with dynamically changing permeabilities due to cycles of fracture-induced dilatancy and healing by mineral precipitation in the actively shearing Grimsel Breccia Fault. These cycles can be induced seismically (e.g., Berger and Herwegh, 2019), which has the following important consequences: (i) the sudden drop in pore fluid pressure results in oversaturation and precipitation of minerals (e.g. quartz, Berger and Herwegh, 2019), and (ii) seismic movements in the fault zone can induce lattice internal damage of apatite grains.

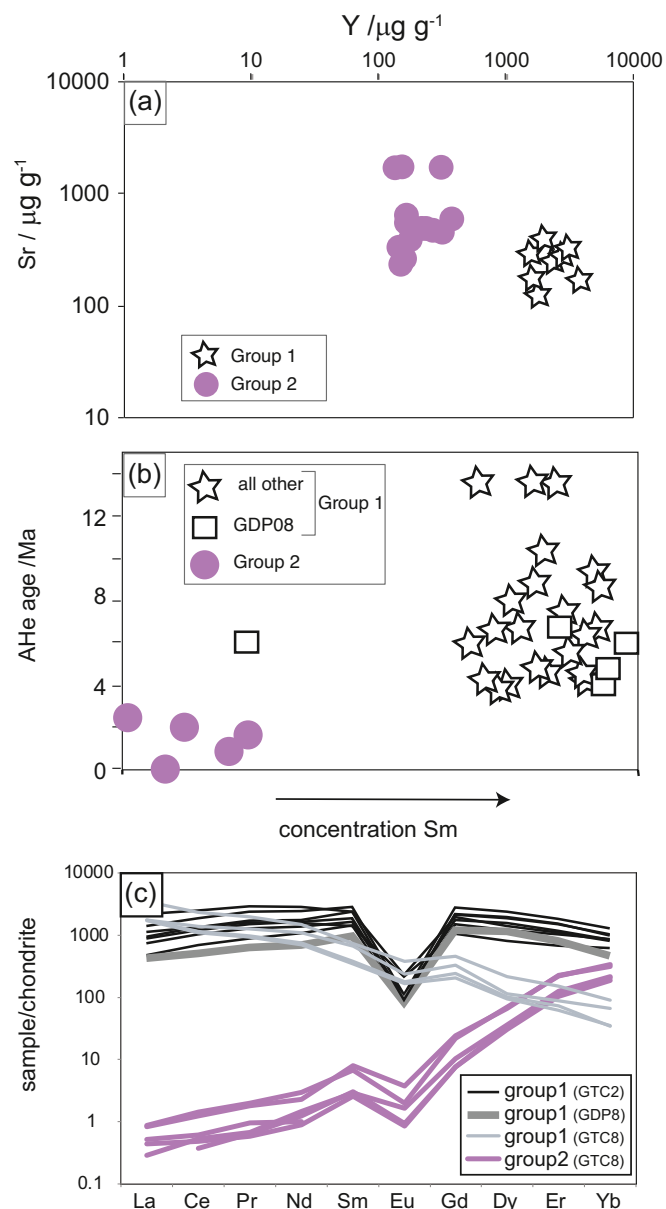


**Fig. 6.** Trace-element characteristics of apatite grains. (a) LA-ICP-MS data for Group 1 samples (GDP08, GTC02) and Group 2 samples (GTC08) characterized by lower Y concentrations and slightly higher Sr contents. (b) Single-grain AHe ages versus the Sm content measured during AHe dating reveal that Group 2 samples have lower Sm content than Group 1 samples, which is consistent with the LA-ICP-MS data. (c) REE pattern of the different apatite samples normalized to chondrite values. Note the prominently different REE patterns between Group 1 and Group 2 apatite.

This geodynamic situation of changing permeability, fluid-pulses and deformation at days/years and/or millions of years time scales can be linked with the AHe ages summarized above. For AHe ages older than the regional cooling ages (Group 3; sample GDP05), infiltration of such grains by upwelling He-bearing fluids and healing of the lattice by apatite precipitation may capture extraneous He. If this occurs below the AHe closure temperature (<60 °C), too old apparent ages will result (Vermeesch et al., 2007; Gautheron et al., 2012; Murray et al., 2014; Zeitler et al., 2017; Recanatia et al., 2017; Milesi et al., 2019, 2020). Apatite grain internal damage and healing is indicated for some investigated examples by cathodoluminescence imaging (see Fig. 4).

For Group 2 apatites, as long as structural damage of apatite is not healed, this may enhance diffusive He-loss, thus potentially resulting in

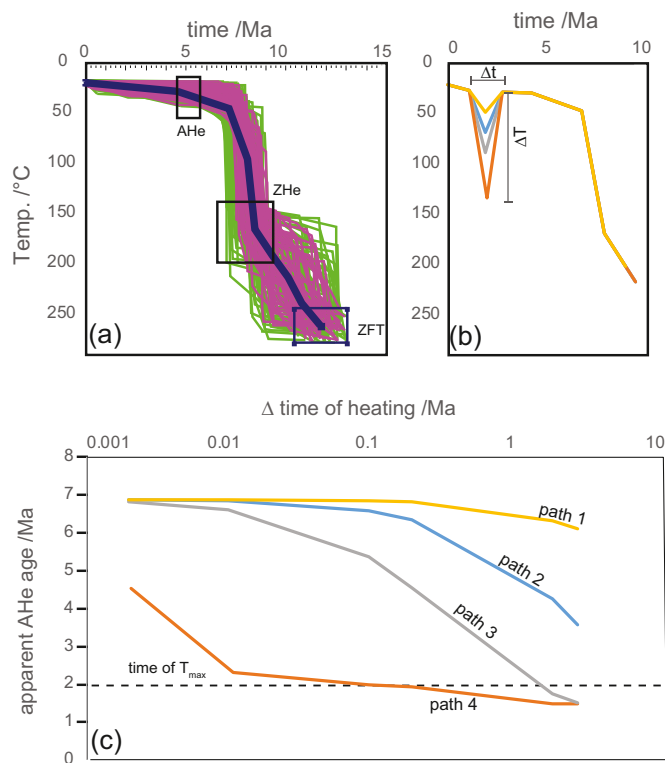


**Fig. 7.** Results of the HeFTy models. (a) Inverse modelling of sample GTC06 (outside the Grimsel Breccia Fault), which is used as the input for the modelling shown in (b + c). Violet lines represent thermal histories with ‘good’ fit to the data (average goodness-of-fit value for all constraints  $>0.5$ ); green lines define thermal histories with ‘acceptable’ fit to the data (average goodness-of-fit value for all constraints  $>0.05$ ; Ketcham, 2005); black line represents best-fitting thermal history and black open box show initial model constraints placed around the thermochronometric ZHe ages; (b) Sketch of different T-t paths (1 to 4, see colour code in c) used as input for the forward HeFTy modelling. (c) Results for the paths 1–4 (colour coding as used in (b), Appendix 3) showing the apparent synthetic AHe ages for different heating durations from hydrothermal activity. (For interpretation of the references to colour in this figure legend, the reader is referred to the web version of this article.)

too young apparent AHe ages. Additionally, aforementioned precipitation/re-crystallization of new apatite grains may occur at temperatures below AHe closure temperatures; hence, apatite in such cases represents a geochronometer and not a thermochronometer. In this case, the average AHe age  $1.48 \pm 0.51$  Ma for sample GTC08 would record a precipitation age. However, the interpretation of single-grain AHe ages as precipitation ages is hampered by the poor knowledge of the temperatures at which this apatite sample crystallised. Chemical modelling of apatite solubility in fluids of the Grimsel Breccia Fault reveals retrograde solubility, thus working against precipitation of apatite by simple cooling. Consequently, another precipitation process is required for apatite. For example, seismic fracturing may promote infiltration and fluid mixing and likely goes along with prominent fluid pressure variations. Alternatively, also aseismic conditions can be envisaged for infiltration of hot hydrothermal water. Such mixing in both cases could be addition of higher temperature hydrothermal fluid into cooler fluid, and the increase in temperature of the mixed fluid could trigger apatite crystallization. In this sense, sudden local changes in the fault’s permeability regime because of earthquake-induced frictional deformation behaviour is more likely than gradual temperature changes.

Our observations and data from the hydrothermally active Grimsel Breccia Fault help to better understand commonly observed over dispersion of low-temperature thermochronological data and also

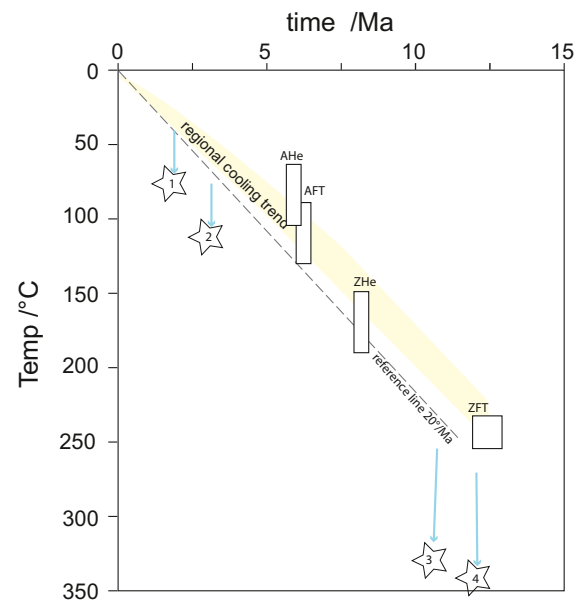


**Fig. 8.** Summary of the available thermochronometric and fluid-influenced data in the Grimsel region. AFT (Vernon et al., 2009; Michalski and Soom, 1990); ZHe (this study), ZFT (Michalski and Soom, 1990). For detailed data and locations see Table 1. Ranges in closure temperatures (rectangular boxes) are taken from Reiners et al. (2018). The fluid-influenced data are: 1: AHe age of sample GTC08 (this study); 2: Ar/Ar age of adularia (Hofmann et al., 2004); 3: Th-Pb monazite ages (Bergemann et al., 2017); 4: Ar/Ar adularia age (Rossi and Rolland, 2014). Blue arrows depict thermal anomalies from regional cooling trend shown as the yellow band. See text for details. (For interpretation of the references to colour in this figure legend, the reader is referred to the web version of this article.)

suggest that under specific conditions the apatite (U-Th)/He system (beside the apatite U-Pb system) can be used as a geochronometer to date apatite crystallization. We therefore suggest that trace element concentrations of apatite grains should be routinely measured in future studies, especially those investigating hydrothermally-affected study areas.

## 6. Summary and conclusions

Along hydrothermally-active faults, different AHe-age behaviour can be observed (see also Milesi et al., 2019, 2020), leading to three general groups of AHe age data: (1) grains which do not record the thermal overprint imposed by (hydro)thermal fluids, (2) AHe ages younger than regional cooling age patterns related to new mineral precipitation/growth with no or very minor diffusional He loss, (3) macroscopically non-visible but frequent fracturing of apatite grains facilitating (diffusive) gain (trapping) or loss of He resulting in apparent AHe ages that are older or rejuvenated.

Apatite microstructures and trace-element compositions can unambiguously identify precipitation and new growth of apatite grains directly from hydrothermal fluid (Fig. 4g) or overgrowth of existing grains (Fig. 4c). For practical reasons (sample preparation and grain selection), only apatite grains with a certain size can be used for AHe dating. Commonly, the link between AHe data and trace elements can be best constrained by the Sm measurement done during the U/Th - He age measurement (see Fig. 6b and c). In order to study the temperature-time evolution in hydrothermal zones, the dynamics of the fluids that might spatially and temporally be more complex as often inferred have to be included. The hydrothermal fluid dynamics have two important effects on the physico-chemical evolution of the apatite grains: (i) solution/precipitation and (ii) changing local temperatures at unknown magnitudes and for unknown durations. These two effects might not be

distinguishable for each single-grain AHe age, but the preservation of regional cooling trends by AHe ages inside fault zones and their co-existence with nearby hydrothermally affected AHe ages documents the high spatial and temporal variability in temperature conditions within such hydrothermal faults. This is corroborated by the missing complete AHe resetting of all fault zone internal apatites, despite the long-lived hydrothermal activity of the entire fault system. In this context, prominent porosity and focused permeability combined with large fluid masses can promote apatite (re)crystallization via fluid mixing and concurrent temperature increase (recall that apatite displays retrograde solubility), the latter possibly linked to seismic events. Detailed studies on apatite microstructures, chemical compositions as well as single-grain (or better in-situ) AHe dispersion therefore represent a tool to unravel a fault's fluid-induced seismic activity.

### Declaration of Competing Interest

The authors declare that they have no known competing interests.

### Acknowledgements

This project is part of the NRP70 program and is funded by the Swiss National Science Foundation (grant number: SNF-407040\_153889). P.G. V. acknowledges funding from the Swiss National Science Foundation (grant PP00P2\_170559) and the French ANR-PIA program (ANR-18-MPGA-0006). This study was carried out within the framework of the Swiss Competence Center for Energy Research – Supply of Energy (SCCER-SoE). We thank Gary O'Sullivan and an anonymous reviewer for their input to clarify the paper.

### Appendix A. Supplementary data

Supplementary data to this article can be found online at <https://doi.org/10.1016/j.chemgeo.2021.120633>.

### References

- Abrecht, J., 1994. Geologic units of the Aar massif and their pre-Alpine rock associations: a critical review: the pre-Alpine crustal evolution of the Aar-, Gotthard- and Tavetsch massifs. *Schweiz. Mineral. Petrogr. Mitt.* 74, 5–27.
- Belgrano, T.M., Herwegh, M., Berger, A., 2016. Inherited structural controls on fault geometry, architecture and hydrothermal activity: an example from Grimsel Pass, Switzerland. *Swiss J. Geosci.* 109, 345–364.
- Belousova, E.A., Griffin, W.L., O'Reilly, S.Y., Fisher, N.I., 2002. Apatite as an indicator mineral for mineral exploration: trace-element compositions and their relationship to host rock type. *J. Geochem. Explor.* 76, 45–69.
- Bergemann, C., Gnos, E., Berger, A., Whitehouse, M., Mullis, J., Wehrens, P., Pettke, T., Janots, E., 2017. Th/Pb ion probe dating of zoned hydrothermal monazite and its implications for repeated shear zone activity: an example from the Central Alps, Switzerland. *Tectonics* 36, 671–689.
- Berger, A., Herwegh, M., 2019. Cockade structures as a paleoearthquake proxy in upper crustal hydrothermal systems. *Nat. Sci. Rep.* 9, 9209.
- Berger, A., Mercolli, I., Gnos, E., 2017. Geological Map of the Aar Massif, Tavetsch and Gotthard Nappes 1:100000. *Landesgeologie der Schweiz*.
- Dempster, T.J., 1986. Isotope systematics in minerals, biotite rejuvenation and exchange during Alpine metamorphism. *Earth Planet. Sci. Lett.* 78, 355–367.
- Dempster, T.J., Jolivet, M., Tubrett, M.N., Braithwaite, C.J.R., 2003. Magmatic zoning in apatite: a monitor of porosity and permeability change in granites. *Contrib. Mineral. Petrol.* 145, 568–577.
- Diamond, L.W., Wanner, C., Waber, H.N., 2018. Penetration depth of meteoric water in orogenic geothermal systems. *Geology* 46 (12), 1063–1066. <https://doi.org/10.1130/G45394.1>.
- Djimbí, D.M., Gautheron, C., Roques, J., Tassan-Got, L., Gerin, C., Simoni, E., 2015. Impact of apatite chemical composition on (U-Th)/He thermochronometry: an atomistic point of view. *Geochim. Cosmochim. Acta* 167, 162–176.
- Egli, D., Glotzbach, C., Valla, P.G., Berger, A., Herwegh, M., 2018a. Low temperature thermochronometry (apatite and zircon (U-Th)/He) across an active hydrothermal zone (Grimsel Pass, Swiss Alps). In: *EGU General Assembly 2018*, 52. Geophysical Research Abstracts, Vienna, pp. 2749–2765.
- Egli, D., Baumann, R., Küng, S., Berger, A., Baron, L., Herwegh, M., 2018b. Structural characteristics, bulk porosity and evolution of an exhumed long-lived hydrothermal system. *Tectonophysics* 747–748, 239–258.
- Flowers, R.M., Ketcham, R.A., Shuster, D.L., Farley, K.A., 2009. Apatite (U+Th)/He thermochronometry using a radiation damage accumulation and annealing model. *Geochim. Cosmochim. Acta* 73, 2347–2365. <https://doi.org/10.1016/j.gca.2009.01.015>, 2009.
- Gautheron, C., Tassan-Got, L., Barbarand, J., Pagel, M., 2009. Effect of alpha-damage annealing on apatite (U+Th)/He thermochronology. *Chem. Geol.* 266, 157–170. <https://doi.org/10.1016/j.chemgeo.2009.06.001>, 2009.
- Gautheron, C., Tassan-Got, L., Ketcham, R.A., Dobson, K.J., 2012. Accounting for long alpha-particle stopping distances in (U-Th-Sm)/He geochronology: 3D modeling of diffusion, zoning, implantation, and abrasion. *Geochim. Cosmochim. Acta* 96, 44–56.
- Glotzbach, C., Reinecker, J., Danicik, M., Rahn, M., Frisch, W., Spiegel, C., 2010. Thermal history of the central Gotthard and Aar massifs, European Alps: evidence for steady state, long-term exhumation. *J. Geophys. Res.* 115, F03017.
- Gorynski, K.E., Walker, J.D., Stockli, D.F., 2014. Apatite (U-Th)/He thermochronometry as an innovative geothermal exploration tool: a case study from the southern Wassuk Range, Nevada. *A. J. Volcanol. Geotherm. Res.* 270, 99–114.
- Harlov, D.H., 2015. Apatite: a fingerprint for metasomatic processes. *Elements* 11, 171–176.
- Henrichs, I.A., O'Sullivan, G., Chew, D.M., Mark, C., Babechuk, M.G., McKenna, C., Emo, R., 2018. The trace element and U-Pb systematics of metamorphic apatite. *Chem. Geol.* 483, 218–238.
- Henrichs, I.A., Chew, D.M., O'Sullivan, G.J., Mark, C., McKenna, C., Guyett, P., 2019. Trace element (Mn-Sr-Y-Th-REE) and U-Pb isotope systematics of metapelitic apatite during progressive greenschist to amphibolite-facies Barrovian metamorphism. *Geochem. Geophys. Geosyst.* 20, 4103–4129.
- Herwegh, M., Kissling, E., Baumberger, R., Berger, A., Wangenheim, C., Wehrens, P., Glotzbach, C., Mock, S., 2020. Late stages of continent-continent collision: timing, kinematic evolution and exhumation of the northern Rim of the Alps. *Earth Sci. Rev.* 200, 102959.
- Hofmann, B.A., Helfer, M., Diamond, L.W., Villa, I.M., Frei, R., Eikenberg, J., 2004. Topography-driven hydrothermal breccia mineralization of Pliocene age at Grimsel Pass, Aar massif, Central Swiss Alps. *Schweiz. Mineral. Petrogr. Mitt.* 84, 271–302.
- Janots, E., Grand'Homme, A., Bernet, M., Guillaume, D., Gnos, E., Boiron, M.-C., Rossi, M., Seydoux-Guillaume, A.-M., De Ascensão Guedes, R., 2019. Geochronological and thermometric evidence of unusually hot fluids in an Alpine fissure of Lauzière granite (Belledonne, Western Alps). *Solid Earth* 10, 211–223, 10.5194/se-10.
- Ketcham, R.A., 2005. Forward and inverse modelling of low-temperature thermochronology data. *Rev. Mineral. Geochem.* 58, 275–314.
- Michalski, I., Soom, M.A., 1990. The Alpine thermo-tectonic evolution of the Aar and Gotthard massifs, central Switzerland: fission track ages on zircon and apatite and K/Ar mica ages. *Schweiz. Mineral. Petrogr. Mitt.* 70, 373–387.
- Milesi, G., Soliva, R., Monié, P., Münch, P., Bellanger, M., Bruguier, O., Bonno, M., Taillefer, A., Mayolle, S., 2019. Mapping a geothermal anomaly using apatite (U/Th)/He thermochronology in the Têt fault damage zone, eastern Pyrenees, France. *Terra Nova* 31 (569–576), 2019. <https://doi.org/10.1111/ter.12429>.
- Milesi, G., Monié, P., Münch, P., Soliva, R., Taillefer, A., Bruguier, O., Bellanger, M., Bonno, M., Martin, C., 2020. Tracking geothermal anomalies along a crustal fault using (U-Th)/He apatite thermochronology and rare-earth element (REE) analyses: the example of the Têt fault (Pyrenees, France). *Solid Earth* 11, 1747–1771. <https://doi.org/10.5194/se-11-1747-2020>.
- Murray, K.E., Orme, D.A., Reiners, P.W., 2014. Effects of U-Th-rich grain boundary phases on apatite helium ages. *Chem. Geol.* 390, 135–151.
- Nibourel, L., Rahn, M., Dunkl, I., Berger, A., Hermann, F., Diehl, T., Heuberger, S., Herwegh, M., 2021. Orogen-parallel migration of exhumation in the eastern Aar Massif revealed by low-T thermochronometry. *J. Geophys. Res. Solid Earth* 126 e2020JB020799.
- O'Sullivan, G., Chew, D., 2020. The clastic record of a Wilson Cycle: evidence from detrital apatite petrochronology of the Grampian-Taconic fore-arc. *Earth Planet. Sci. Lett.* 552, 116588.
- O'Sullivan, G., Chew, D., Kenny, G., Henrichs, I., Mulligan, D., 2020. The trace element composition of apatite and its application to detrital provenance studies. *Earth Sci. Rev.* 201, 103044.
- Pfeifer, H.R., Sanchez, A., Degueldre, C., 1992. Thermal springs in granitic rocks from the Grimsel Pass (Swiss Alps): the late stage of a hydrothermal system related to Alpine Orogeny. In: Kharaka, Y.K., Maest, A.S. (Eds.), *Proceedings of Water-Rock Interaction WRI-7*. A.A. Balkema, Rotterdam, The Netherlands, Park City, Utah, pp. 1327–1330.
- Recanatia, A., Gautheron, C., Barbarand, J., Missenard, Y., Pinna-Jamme, R., Tassan-Got, L., Carter, A., Douville, E., Bordier, L., Pagel, M., Gallagher, K., 2017. Helium trapping in apatite damage: Insights from (U-Th-Sm)/He dating of different granitoid lithologies. *Chem. Geol.* 470, 116–131.
- Reiners, P.W., Brandon, M.T., 2006. Using thermochronology to understand orogenic erosion. *Annu. Rev. Earth Planet. Sci.* 34, 419–466.
- Reiners, P.W., Carlson, R.W., Renne, P.R., Cooper, K.M., Granger, D.E., McLean, N.M., Schoene, B., 2018. *Geochronology and Thermochronology*. Wiley, Hoboken, p. 464.
- Rolland, Y., Cox, S.F., Corsini, M., 2009. Constraining deformation stages in brittle-ductile shear zones from combined field mapping and <sup>40</sup>Ar/<sup>39</sup>Ar dating: the structural evolution of the Grimsel Pass area (Aar Massif, Swiss Alps). *J. Struct. Geol.* 31, 1377–1394.
- Rossi, M., Rolland, Y., 2014. Stable isotope and Ar/Ar evidence of prolonged multi-scale fluid flow during exhumation of orogenic crust: example from the Mont Blanc and Aar Massifs (NW Alps). *Tectonics* 33, 1681–1709. <https://doi.org/10.1002/2013TC003438>.
- Shuster, D.L., Flowers, R.M., Farley, K.A., 2006. The influence of natural radiation damage on helium diffusion kinetics in apatite, *Earth Planet. Sci. Lett.* 249, 148–161. <https://doi.org/10.1016/j.epsl.2006.07.028>.

- Sonney, R., Vuataz, F.-D., 2008. Properties of geothermal fluids in Switzerland: a new interactive database. *Geothermics* 37 (5), 496–509. <https://doi.org/10.1016/j.geothermics.2008.07.001>.
- Valla, P.G., van der Beek, P., Shuster, D.L., Braun, J., Herman, F., Tassan-Got, L., Gautheron, C., 2012. Late Neogene exhumation and relief development of the Aar and Aiguilles Rouges massifs (Swiss Alps) from low-temperature thermochronology modeling and  $4\text{He}/3\text{He}$  thermochronometry. *J. Geophys. Res.* 117, F01004. <https://doi.org/10.1029/2011JF002043>.
- Valla, P.G., Rahn, M., Shuster, D.L., van der Beek, P.A., 2016. Multi-phase late-Neogene exhumation history of the Aar massif, Swiss central Alps. *Terra Nova* 28, 383–393.
- Vermeesch, P., Seward, D., Latkoczy, C., Wipf, M., Günther, D., Baur, H., 2007. A-emitting mineral inclusions in apatite, their effect on (U–Th)/He ages, and how to reduce it. *Geochim. Cosmochim. Acta* 71, 1737–1746.
- Vernon, A.J., van der Beek, P.A., Sinclair, H.D., Persano, C., Foeken, J., Stuart, F.M., 2009. Variable late Neogene exhumation of the central European Alps: low-temperature thermochronology from the Aar Massif, Switzerland, and the Lepontine Dome, Italy. *Tectonics* 28, TC5004.
- Waber, H.N., Schneeberger, R., Mäder, U.K., Wanner, C., 2017. Constraints on evolution and residence time of geothermal water in granitic rocks at Grimsel (Switzerland). *Proc. Earth Planet. Sci.* 17, 774–777. <https://doi.org/10.1016/j.proeps.2017.01.026>.
- Wagner, G.A., Reimer, G.M., Jäger, E., 1977. Cooling ages derived by apatite fission track, mica Rb–Sr and K–Ar dating: the uplift and cooling history of the central Alps. *Inst. Geol. Mineral. Univ. Padova Mem.* 30, 1–27.
- Wanner, C., Diamond, L.W., Alt-Epping, P., 2019. Quantification of 3-D thermal anomalies from surface observations of an orogenic geothermal system (Grimsel Pass, Swiss Alps). *J. Geophys. Res. Solid Earth* 124, B018335.
- Wehrens, P., Berger, A., Peters, M., Spillmann, T., Herwegh, M., 2016. Deformation at the frictional-viscous transition: evidence for cycles of fluid-assisted embrittlement and ductile deformation in the granitoid crust. *Tectonophysics* 693, 66–84.
- Wehrens, P., Baumberger, R., Berger, A., Herwegh, M., 2017. How is strain localized in a meta-granitoid, mid-crustal basement section? Spatial distribution of deformation in the central Aar massif (Switzerland). *J. Struct. Geol.* 94, 47–67.
- Whipp, D.M., Ehlers, T.A., 2007. Influence of groundwater flow on thermochronometer-derived exhumation rates in the central Nepalese Himalaya. *Geology* 35, 851–854.
- Zeitler, P.K., Enkelmann, E., Thomas, J.B., Watson, E.B., Ancuta, L.D., Idleman, B.D., 2017. Solubility and trapping of helium in apatite. *Geochim. Cosmochim. Acta* 209, 1–8. <https://doi.org/10.1016/j.gca.2017.03.041>, 2017.